Eberhard Karls University Tübingen
Department of Physics

BACHELOR THESIS

Implementation of a cross correlation function for coded mask imaging on an FPGA platform

by

Ulrich Baehr

supervisor

Prof. Andrea Santangelo

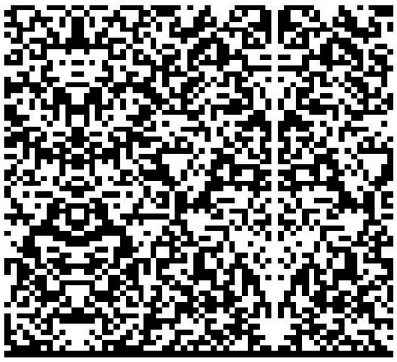

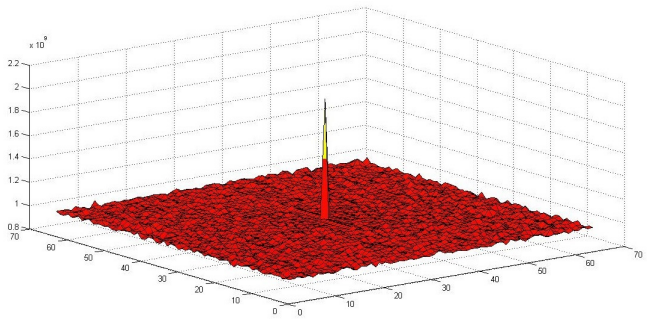

Institute of Astronomy and Astrophysics

June 2015

Abstract

Coded mask imaging is a technique providing vast possibilities and advantages in X-ray astronomy, in comparison to direct imaging telescopes. But it also requires additional computational effort for obtaining a proper sky image, since the incoming photons are encoded with a mask pattern and therefore includes appropriate decoding after the detection.
This bachelor thesis is dedicated to implement a simple design for the decoding process of a coded mask system, which could be used for later developments of planned satellite missions. A possible candidate is the Large Observatory for X-ray Timing (LOFT) mission, which was proposed as M4 mission candidate, with its Wide Field Monitor (WFM) coded mask system.
The design includes the complete decoding process and the communication via an USB interface and also the production and test of several coded masks. The design was coded for a Virtex 4 FPGA by using the hardware description language VHDL and the the Ip-core library of Xilinx.

Introduction

A new age of multiwavelength astronomy had begun, as the technical advance of the 20th century enabled the launch of spaceflight observatories. Especially the exploration of high energy sources emerged quickly, starting with the first rocket mission after the second world war.

In 1949 the sun was observed as the first astronomical X-ray source by the Naval Research Laboratory[1]. It took over twenty years until the first X-ray satellite UHURU[2] was launched in 1970 and started the first all sky X-ray survey. At the end of the century more than 150.000 X-ray sources had been discovered by the High Energy Observatory (HEOA)[3] 1 and 2, operating in the late 70s, and ROSAT[4], which was launched in 1990.

This breakthrough was enabled by a new type of focussing technique for X-rays, the Wolter mirror[5] which is also deployed in the largest X-ray satellites today, the CHANDRA Observatory and XMM Newton, and will also be used by the ESAs upcoming mission ATHENA.

For higher energies and wide angle observations another type of telescope was first successfully applied at the BeppoSAX mission in 1996. Its special part is a mask, which encodes the sky image on a detector plane and is therefore called coded mask telescope. It took only six months for this new instrument to prove its usefulness, as BeppoSAX[6] provided for the first time a fast and precise enough identification of very bright, short duration gamma ray flashes called Gamma Ray Bursts (GRBs), to prove their extragalactic origin. Today coded mask systems have become standard for X-ray astronomy and are used on recent missions as IBIS on Integral[7] and the BAT at the Swift[8] mission.

The extensive computational effort necessary in order to obtain proper sky images from this kind of telescope system prevented the development of onboard decoding processes until the last decade, as the electronic development led to many improvements for modern CPUs and FPGAs[9]. This bachelor thesis shall prove, that its possible to implement the detection procedure for coded mask telescopes on FPGA platforms within an acceptable processing speed for onboard application.
The implemented design leads to the capability of detecting gamma-ray bursts in a shorter time than previous designs for future satellite missions as the proposed LOFT satellite with its Wide Field Monitor (WFM)[10].

The work of this bachelor thesis includes the implementation of the the whole decoding process and the communication between PC and FPGA on a Virtex 4 FPGA-board, as well as the design of several coded mask patterns. Additionally, a 64×64 Pixel low energy X-ray detector has been used to test the behaviour and performance of the detection algorithm with three different mask-patterns. The mask-patterns were implemented with Matlab, which was also used for reference results.

A brief review of the LOFT mission, especially of the WFM and its observational objects will be given in Chapter 1. Chapter 2 includes an overview of the astronomical sources for coded mask imaging. The theoretical background of coded mask imaging will be described in Chapter 3. Chapter 4 is dedicated to explain how the basic program structure is designed. The test results of the simulations as well as the detector data are shown and discussed in Chapter 5 and finally a discussion of the results and possible improvements as an outlook will be given in the concluding Chapter 6.

[1] [Friedman, 1951]
[2] [Jagoda, 1972]
[3] [Peterson, 1975]
[4] [Barstow M. et al, 1990]
[5] [Wolter Hans, 1952]
[6] [Amati, L, 2003]
[7] [Ubertini *et al.*, 2003]
[8] [Barthelmy *et al.*, 2005]
[9] Field Programmable Gate Arrays (FPGAs) are integrated circuits, that are designed to be configured by a programmer after manufacturing.
[10] [Brandt S. et al, 2014]

Contents

1 The LOFT mission **6**
- 1.1 The Large Area Detector . . . 6
- 1.2 The Wide Field Monitor . . . 7

2 Astronomical sources for coded mask telescopes **9**
- 2.1 Gamma Ray Bursts . . . 9
- 2.2 Other transient sources . . . 9

3 Coded mask imaging **12**
- 3.1 The advantage of coded mask systems . . . 12
- 3.2 Principle of Detection . . . 14
- 3.3 Optical design . . . 14
- 3.4 The Design of a coded mask . . . 16
  - 3.4.1 The MURA Mask . . . 17
  - 3.4.2 The m-sequence Mask . . . 17
  - 3.4.3 The Single Pinhole Mask . . . 18
- 3.5 Image reconstruction theory . . . 18
  - 3.5.1 Matched cross correlation . . . 18
  - 3.5.2 Mismatched cross correlation . . . 19
  - 3.5.3 Balanced cross correlation . . . 19
  - 3.5.4 Cross correlation via the Fast Fourier Transform . . . 20

4 Hardware development **22**
- 4.1 Implementing the cross correlation for an FPGA . . . 22
  - 4.1.1 Clocking and Reset-management . . . 22
  - 4.1.2 Communication Interface . . . 22
  - 4.1.3 Data preprocessing and RAM Management . . . 22
  - 4.1.4 The FFT cross correlation . . . 23
- 4.2 Matlab implementation for reference results . . . 26
  - 4.2.1 Mask Designs for the test setup . . . 26

5 Validation and Testing **27**
- 5.1 Autocorrelation functions of different Masks . . . 27
  - 5.1.1 The m-sequence Mask . . . 27
  - 5.1.2 The MURA Mask . . . 28
  - 5.1.3 The single pinhole Mask . . . 28
- 5.2 Correlation Results for different masks . . . 29
  - 5.2.1 The m-sequence Mask . . . 30
  - 5.2.2 The MURA Mask . . . 31
  - 5.2.3 The Pinhole Mask . . . 31
- 5.3 Test Results for processing speed . . . 32

6 Outlook **33**

1 The LOFT mission

The Large Observatory for X-ray Timing is an X-ray mission, which was first proposed to be launched in 2024 for the M3 slot of the ESAs Cosmic Vision Program, but was not selected. The LOFT consortium has decided to re-propose the mission for the M4 slot and to continue its technical development.
The scientific goals of LOFT are the observation of compact objects like super-massive black holes, neutron star systems and black hole binaries in order to study strong gravitational fields and the equation of state of neutron stars. They can be achieved by the measurement of the spectral variability of the X-ray flux emitted by matter very close to compact objects and will be enabled by the LOFTs main instrument, the Large Area Detector (LAD).
The Wide Field Monitor, LOFTs secondary instrument is mainly designed to select observational targets for the LAD, but also has the capability to carry out scientific investigations on its own. The facts presented in the Chapter are based on the articles of [Zane S., 2014].

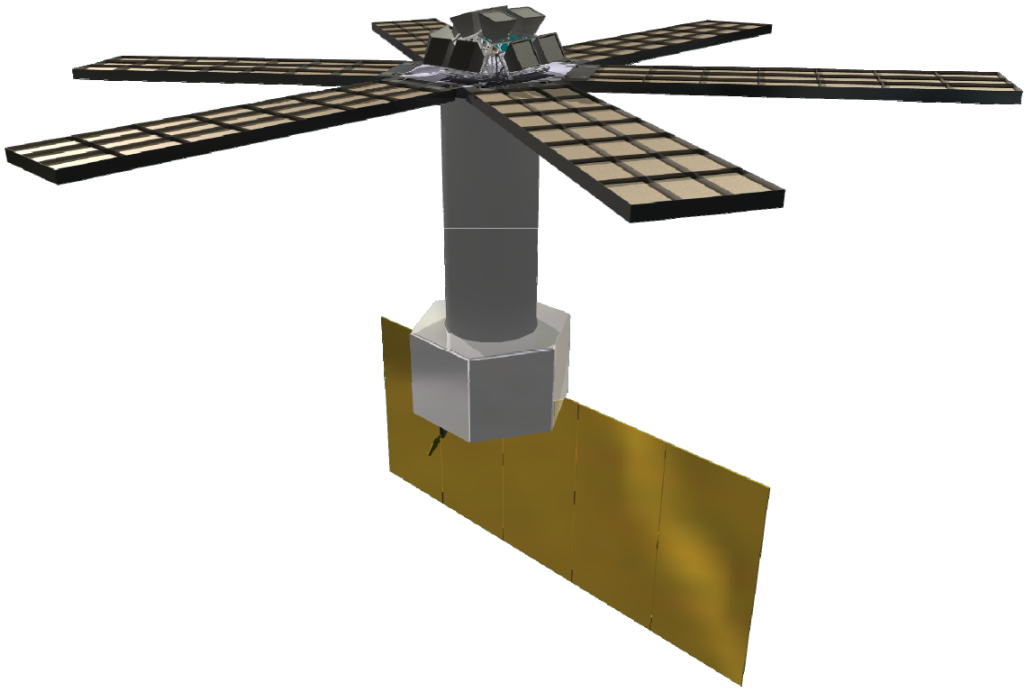

Figure 1: The LOFT mission concept showing the six LAD-panels as well as the Wide Field Monitor in the center and the solar panel at the bottom. *(Image and source: [Brandt S. et al, 2013])*

1.1 The Large Area Detector

The LAD is a collimated instrument with a narrow FoV (1°) and an effective area of $9,5\,\mathrm{m}^2$ at 6 keV, separated in six modules, which is more than 15 times larger than any other previous flown X-ray instrument (compare Figure 1). With a spectral resolution of 260 eV and a timing resolution better than $10\,\mu$s the LAD will operate within the energy range of $2-30$ keV.
In order to provide this large area payload without exceeding weight constrains, innovative Silicon Drift Detectors (SDDs) will be applied combined with a collimator-system consisting of lead glass microchannel plates [Zane S. et al, 2014].

1.2 The Wide Field Monitor

The secondary instrument of LOFT is the Wide Field Monitor. It consists of five pairs of coded mask instruments (compare Figure 2) and will be discussed in greater detail as this thesis is originally dedicated to contribute to its further development.
Its primary purpose is to detect transient sources and emission state changes of known X-ray sources and select them as observation targets for the LAD. Additionally the WFM is equipped to perform observations on its own due to its high duty cycle.
With an extremely large FoV, the WFM covers over 1/3 of the whole sky and is therefore well suited to detect and identify bright short duration events like Type 1 X-ray burst, Soft Gamma Repeaters (SGRs) and Gamma Ray Bursts (GRBs). The source location accuracy of 1 arcmin and the wide energy range of $2 - 50\,\mathrm{keV}$ combined with a spectral resolution of $300 - 500\,\mathrm{eV}(10\,\mu\mathrm{s})$ allow the WFM to observe GRBs with excellent precision. At least 100 GRB detections per year are expected [Brandt S. et al, 2014].
A real time burst alert system will be implemented and built, allowing the WFM to send the location and trigger time of a detected impulsive event within 30 s [Schanne Stephane. et al, 2014].
Beneath the monitoring of long term flux variation of known X-ray sources the WFM will also contribute to the exploration of X-ray flashes, mainly produced by supernovae shock break-outs.

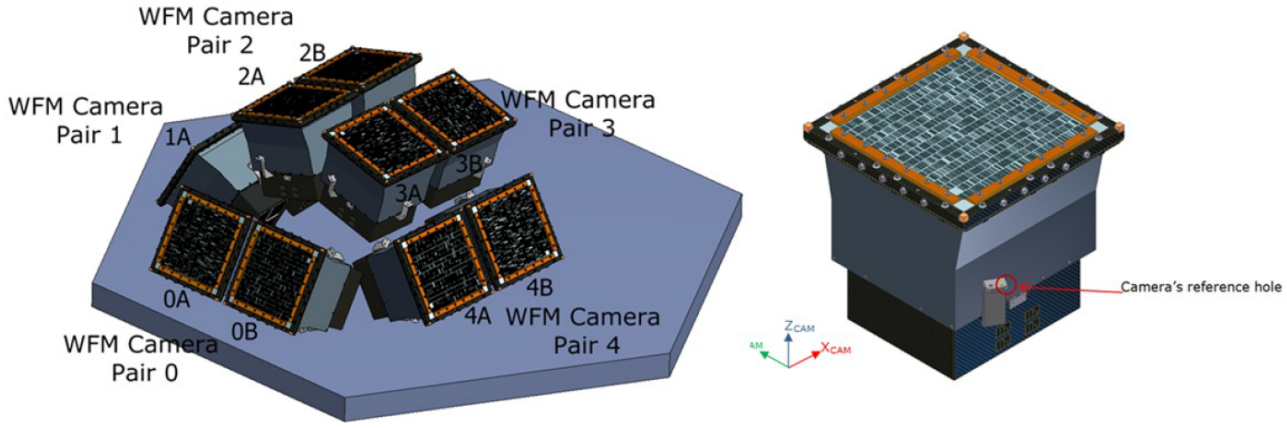

Figure 2: The WFM with its five camera-pairs installed on an optical bench on the left. A single camera setup is shown on the right. The WFM is protected by a sun light shield (not shown).*(Image and source: [Brandt S. et al, 2014])*

The WFM cameras are equipped with Silicon Drift Detectors similar to the LAD. As one SDD anode has an elongate rectangle shape instead of the square shape of a pixel, the detector position resolution is much more precise in one direction ($< 60\,\mu$m) than in the other ($< 8\,$mm). The result is an elongated point spread function in one direction, but is matched by the co-alignment of two cameras rotated (90°) with respect to each other (compare Figure 3). The combined sky image achieves the targeted 1 arcmin resolution and covers a $90° \times 90°$ area.

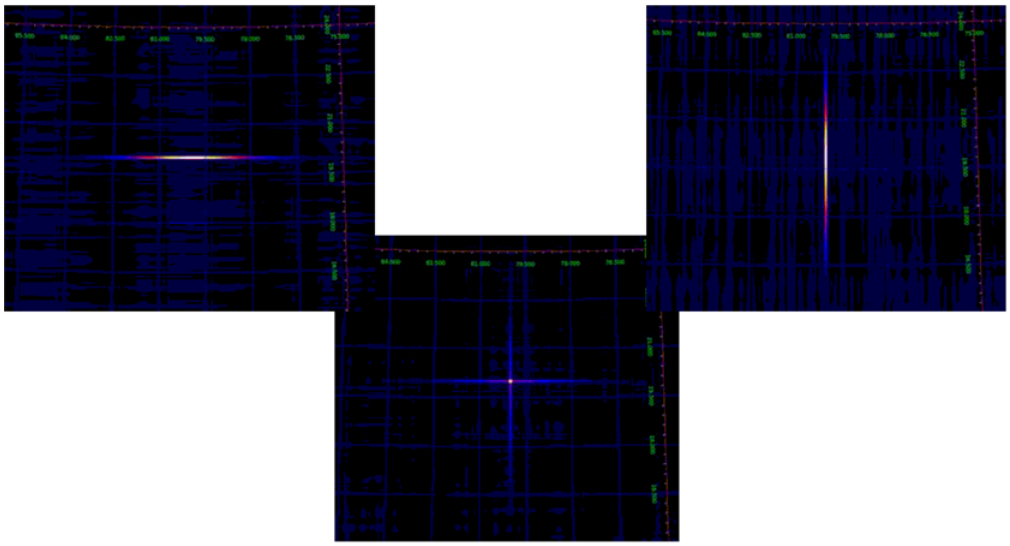

Figure 3: A simulated single point-source was used to produce the upper images of the single cameras. The combination of the two images results in the lower picture. The images only show 10 % of the systems FoV.

The Loft Burst On-board Trigger system (LBOT) is responsible for the detection of new burst like events and produces the alert message sequence, containing the source position. Two different trigger types are implemented:

1. an image trigger for long term events, which produces a sky image every 20 s.
2. a count-rate increase trigger for short term events (below 20 s), which selects the timing-window within a GRB candidate is detected for immediate sky image decoding.

Both triggers are implemented for every camera of the WFM. The combination of a camera pair instead of single cameras allows the identification of much fainter sources, thanks to the possibility of coincidence detection between both cameras [Brandt S. et al, 2014].

2 Astronomical sources for coded mask telescopes

Impulsive fast events as X-ray bursts and especially Gamma Ray Bursts are the most important class of sources coded mask telescopes are designed to observe, due to their comparable large Field of View and sufficient angular resolution.
But also other transient sources, such as X-ray Binaries or Pulsars are objects, that can be observed reasonably well with coded mask systems. Their main characteristic, a time dependant flux, makes them interesting for long time observations, which is easier to perform with a large Field of View instrument, as many of these sources can be observed simultaneously. The content of this Chapter is based on the book of F.D. Seward 2010.

2.1 Gamma Ray Bursts

Gamma Ray Bursts (GRBs) are short term flashes with a time-scale from a few seconds up to several minutes, with extremely high intensity in the high energy X-ray range. They are the brightest electromagnetic events being detected so far. The burst itself can past from several seconds up to several minutes. The afterglow can be observed in lower energy ranges for several hours.
The Vela-satellites, originally designed to detect gamma rays emitted by nuclear weapon tests, randomly observed the first GRBs in the late 60s. It remained unclear if these events are extragalactical origin until the Burst and Transient Source Experiment (BATSE) on NASAs CGRO was launched and able to measure over 2700 Bursts within nine years (compare Figure 4). The distribution of the events is highly isotropic, which excluded the possibility of a solely galactic origin, but it remained unclear from where these events are coming and how they are produced [Seward F.D. Charles P.A. , 2010].
In May 1997 the Gamma Ray Burst Monitor of the Italian satellite BeppoSax detected a burst, that was later called GRB970508, and sent the position to earth with an Error-Box[1] small enough for follow up observation in the optical energy range. For the first time the afterglow was observed and a faint distant galaxy was identified as origin.
The knowledge of the source distance brought up another problem. The calculated set free energy of the brightest GRBs exceeded 10^{54} erg given an isotropic emission, which is within the range of the solar mass energy equivalent. Despite several follow up missions as the Burst Alert Telescope on the SWIFT-satellite or NASAs FERMI-satellite, it is still not clear which events are responsible for these massive outbursts. So further observations with better instruments, as for example the WFM, are necessary to achieve a better understanding of these spectacular events.

2.2 Other transient sources

Transient sources is the collective term for objects or phenomena with a time dependant emission rate, that is either periodic or burst like. The duration reaches from seconds to months or even years. This behaviour makes them interesting for long term observations. Typical candidates are X-ray binaries and pulsars.

Binary systems are two objects orbiting around one common gravitational center. If these objects are close enough, matter accretion from one star to the other can occur. If the accreting star is a compact object, X-ray or even Gamma ray emission is released as thermal radiation

[1] As every telescope has a precision limit, the Error-Box gives a potential position area of a source within a certain probability.

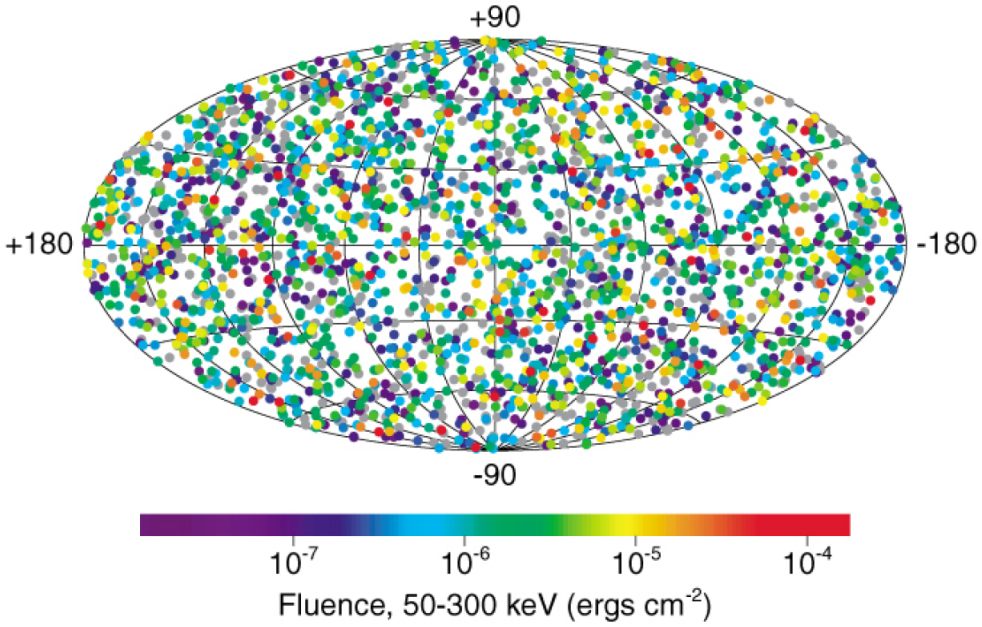

Figure 4: The distribution of 2704 GRBs observed by BATSE over the complete sky. The integrated flux of each event is scaled in colours from purple to red. The positional distribution is too homogeneous for events solely produced from our galaxy, as there is no accumulation of sources around the galactic plane. *(Image and source: NASA)*

from its accretiondisk or surface.
X-ray Binaries are generally divided into two classes dependant of the mass relation between the compact object and the companion star (compare Figure 5).

1. High mass X-ray Binaries (HMXB) have very massive companion stars. Parts of the stellar wind of these companions are pulled into the gravitational field of the compact object, which is called stellar wind accretion.

2. Low mass X-ray Binaries (LMXB) have main sequence stars of white dwarf companions. If the radius of the companion exceeds the equipotential gravitational point between the two objects, matter can be transferred to the compact object. This mechanism is called Roche-lobe[1] overflow. A subclass of LMXBs are cataclysmic variables (CV), which are low mass X-ray Binaries with white dwarfs as the primary star, that increase their brightness infrequently. Two different mechanisms lead to this behaviour. Nova bursts are produced by instabilities of the accretion disk, when a part of the disk directly falls on the surface of the white dwarf. The brighter and less frequent classical novae occur when the bottom temperature of the accreted hydrogen layer on the surface of the white dwarf is hot enough to trigger a runaway hydrogen fusion reaction.

[1]The Roche-lobe is defined as the region around the star of a binary system within which orbiting matter is gravitationally bound.

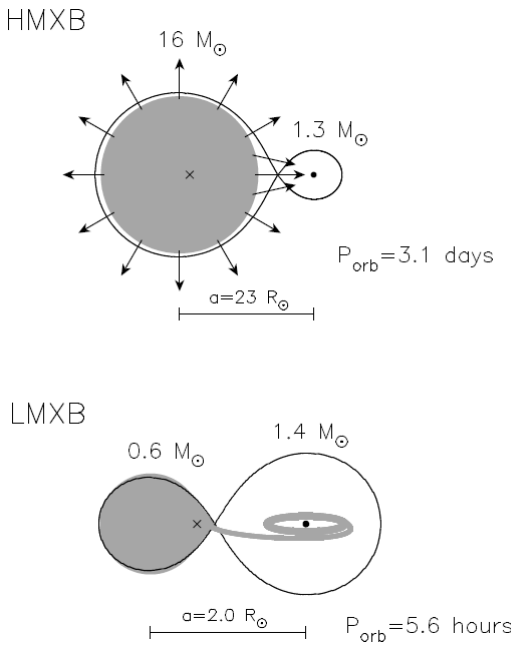

Figure 5: The image shows a typical HMXB system at the top and an LMXB at the bottom *(Image: [Tauris & van den Heuvel, 2006])*

Pulsars are neutron stars with their magnetic axes not aligned to the rotation axes, emitting a strong beam of X-rays. The beam can only be observed when the emission direction is directly pointing towards the earth, similarly to a lighthouse, that can only be seen when it points to the observer. Therefore, the emission appears highly periodic, as neutron stars have short, regular rotation periods from milliseconds to seconds. The driving mechanism behind the X-ray emission are either accretion (in binary systems) or rotation (in isolated systems). Accreted matter cannot fall directly onto the surface of the neutron star, due to angular momentum conservation. The matter is ionized by the high temperatures due to friction in the accretion disk and couples with the neutron stars magnetic field lines. On the magnetic poles the protons and electrons reach the surface and produce a strong thermal emission in the X-ray energy range. Even higher energies are reached due to inverse Compton scattering with the down falling electrons.

3 Coded mask imaging

3.1 The advantage of coded mask systems

Studying astrophysical X-ray sources brings a significant amount of technical difficulties, due to the physical properties of x-rays. As photons start to scatter randomly at energies above 1 keV and only reflect within very small angles, classical mirror-optics cannot be used for focusing purposes. The Wolter mirrors, which reflect X-rays within an angle smaller than 1 ° to the surface achieve excellent angular resolution, but have the disadvantage of a big focal length, and a comparable small Field of View. The NASAs CHANDRA mission for example already uses a Wolter mirror of 10 m focal length in order to observe X-ray sources up to 10 keV within a FoV of $0,5$ ° (compare Figure 6). The focal length needed for energies of 40 keV and above makes is virtually impossible to build focussing-optics for space applications.

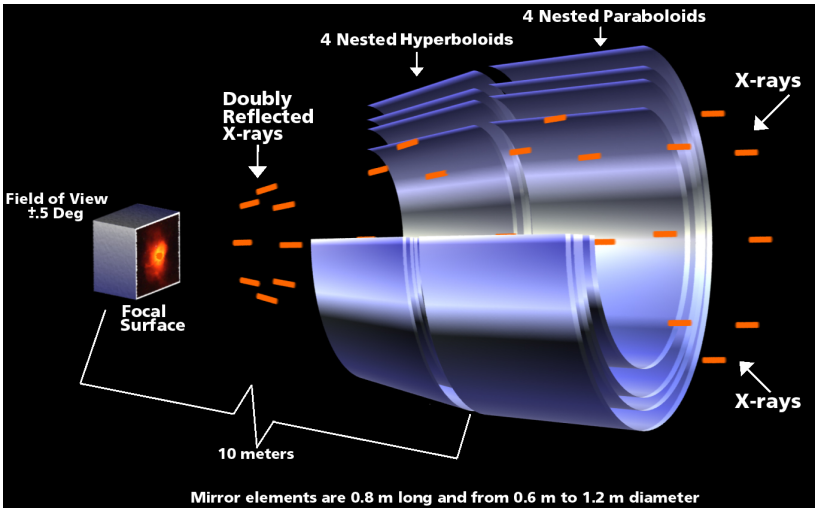

Figure 6: With a length of 10 m and a diameter of 1.2 m the CHANDRA telescope reaches a FoV of $0,5$°.[Kimberly Kowal Arcand, 2012]

Another, simpler method is the use of collimators to shrink the FoV and therefore achieve a better angular resolution. The collimators block incoming flux from the sides, while flux within the opening angle α hits the detector unhindered (compare Figure 7).
The disadvantage here is the loss of flux due to the shading of the collimator-array on the detector-plane. Besides, a better angular resolution always means a smaller FoV.

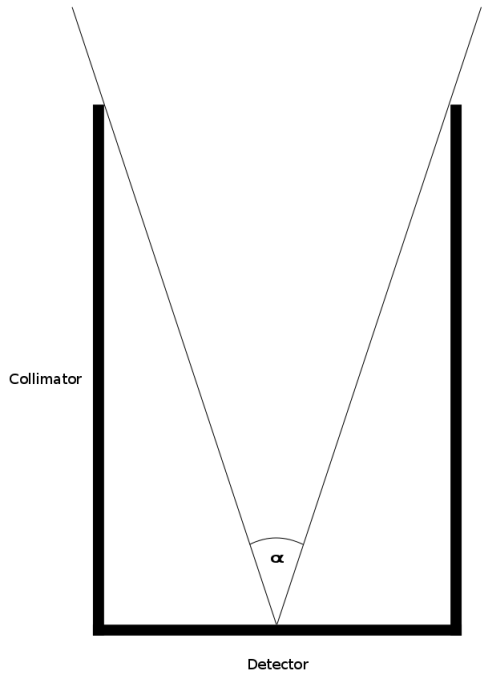

Figure 7: The angular resolution α depends on the ratio between detector- and collimator length.

Coded mask telescopes achieve angular resolutions down to a few arcmins, while having a wide FoV and are able to operate on higher energies than any satellite compatible Wolter telescope can reach.

The Burst Alert Telescope (BAT) on the Swift satellite for example exploits the large FoV ($1,4\,\mathrm{sr}$ half-coded $2,3\,\mathrm{sr}$ partially coded) paired with a fine angular resolution (17 arcmin) and an energy-range up to 150 keV [Barthelmy *et al.*, 2005]. The IBIS Instrument on the INTEGRAL-mission achieves an even higher angular resolution (12 arcmin) with an energy-range from 15 keV up to 10 MeV at the cost of a slightly smaller FoV (9° full coded 19° half coded) [Ubertini *et al.*, 2003].

But these advantages come with a substantial trade off. The computational effort for the sky image reconstruction makes it challenging to implement designs for onboard devices.

3.2 Principle of Detection

A coded mask telescope consists of a detector plane and a mask with the coded pattern, which is installed in front of the detector. The distance between mask and detector is determined by the specific setup and the dimensions of the detector plane. The single pixels of the mask are either opaque or transparent and are distributed in special patterns, which will be discussed in chapter 3.4. If we consider a point source flux hitting the aperture, the photons will be blocked by the opaque pixels, therefore the mask pattern is projected directly on the detector plane. So for several sources the detector would be hit by overlapping distributions of the mask shadow (compare Figure 8).

The resulting encoded image now needs to be decoded to retain the correct sky image. This

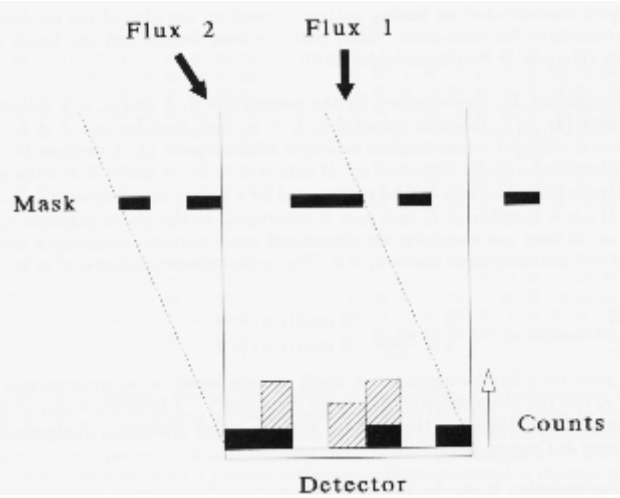

Figure 8: The stacking of photons per pixel from different sources demands proper decoding.[Zand, Johannes Joseph Marie in 't, 1992]

will be explained in Chapter 3.5. One also has to consider that every imaged point source experiences the noise of the whole detector while with focussing techniques only a small part of the detector is contributing. Therefore, the sensitivity of the instrument, will always be better with focussing techniques provided the use of equal collection areas.

3.3 Optical design

The optical design of the system depends on the mask- and detector size, the size of the mask-pattern, the distance between mask and detector, and the size and position of an optional collimator on the detector plane. It directly dictates the image quality, the angular resolution and the Field of View. The Field of View (FoV) is defined by the ratio of the size of mask and detector and also the distance between them. The FoV is divided in the fullcoded Field of View (FCFV) and the partially coded Field of View (PCFV) as shown in Figure 9.

Two basic designs are possible. The so called the simple design, which uses the same size for mask and detector and the optimum designs shown in Figure 10. While the simple design works well without a collimator, a proper shielding is necessary to stop incoming flux from the sides. The FCFV as well as the PCFV are smaller compared to the optimum designs. Additionally off-axis sources will produce sidelobe peaks to some extend[Zand, Johannes Joseph Marie in 't, 1992].

The optimum design has two types, one with a smaller mask compared to the detector-plane and one with a larger mask. A design with a smaller mask than the detector restrains the FCFV while the PCFV remains large. A setup with a larger mask than the detector-plane is called

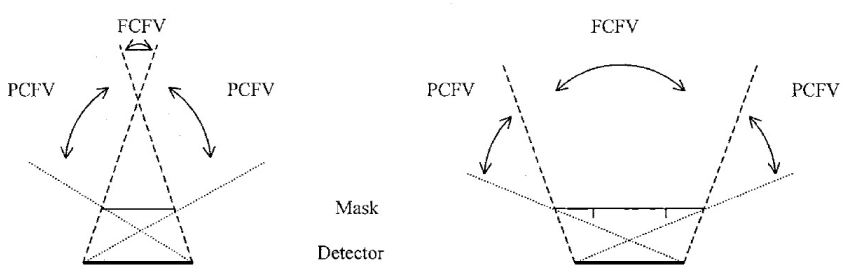

Figure 9: The left figure shows a setup with a smaller Mask and therefore a small FCFV. The right figure shows the optimum cyclic setup, which has become the standard due to its large FCFV.

cyclic and is by far the most common, because of its large FCFV. Normally, this design is built with a collimator in order to confine the FOV to the FCFV.[Roberto Accorsi, 2001]

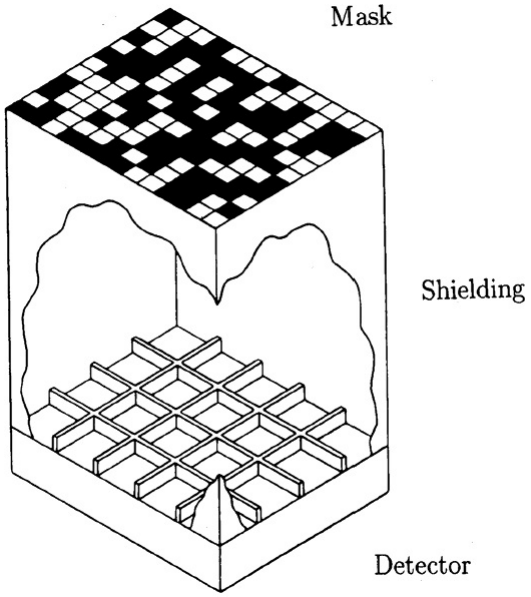

Figure 10: In the simple design the collimator is replaced by a simple shield that prevents incoming photons which are not modulated by the mask[Dean, 1983].

3.4 The Design of a coded mask

In order to achieve good imaging quality, a mask pattern has to fulfil the following conditions:

1. the autocorrelation-function, which is the result of an mask-pattern correlated with itself, should be a delta function at the center with perfect flat side lobes [Roberto Accorsi, 2001]
2. the signal to noise ratio of the coded sky image should be optimum
3. a grid needs to be implemented to hold free opaque elements together or they should be avoided
4. the ratio between transparent and opaque elements should ideally be $1:1$

At the early stages of coded mask imaging two types of patterns were proposed: the random pinhole pattern and a pattern of Fresnel zones. Both designs are not ideal in concern of the first condition. The sidelobes of the autocorrelation-function are not flat for both types. Therefore so called artefacts will occur.

Today several other mask-patterns are well known and in common use:

1. the modified uniformly redundand array (MURA mask)
2. the m-sequence arrays (M-mask or LFSR mask)
3. the random mask
4. single pinhole mask

3.4.1 The MURA Mask

Gunson Polychronopulos found an almost perfect pattern by using cyclic difference sets in 1976: A cyclic difference set modulo k is basically a set of n positive numbers $a_1, a_2, ..., a_n$ smaller than k. They have the property that all differences d between a_i and a_j modulo k for $i \neq j$ are different. This behaviour ensures that no pattern repeats itself within modulo k. Additionally, a_i has the very useful characteristic that every difference $i - j$ between a pair $a_i, a_j = 1$ is equally sampled, which perfectly fulfils requirement 4. Therefore these sets are also called modified uniformly redundant arrays (MURAs)[R. J. Procter, G. K. Skinner, A. P. Willmore, 1978].

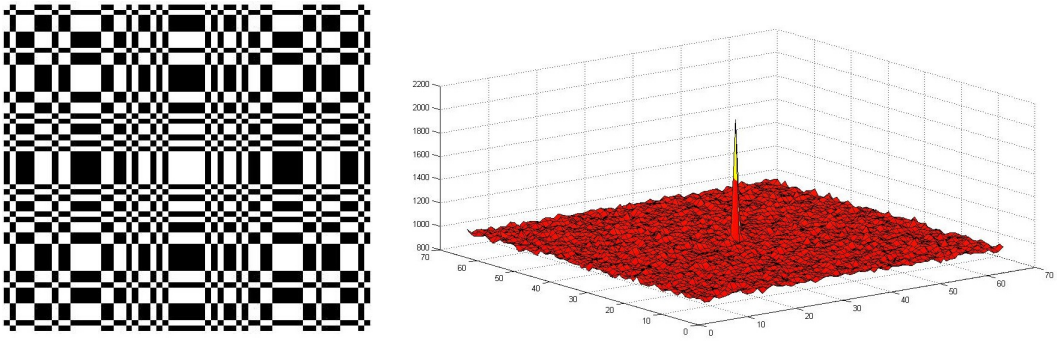

Figure 11: A classical MURA mask with 61×63 element size. The same pattern was used for the IBIS instrument on the Integral mission. Note the near perfect autocorrelation.

3.4.2 The m-sequence Mask

Another way to produce an optimum mask pattern is the usage of so called m-sequence-arrays (maximal-length linear feedback shift register sequence). A linear feedback shift register (LFSR) with a length of m produces a non redundant sequence of the length 2^{m-1} without the "zero-vector". This sequence can also be represented as a set of irreducible polynomial of degree m of coefficients $p_1, p_2, ..., p_{m-1}$ where $p \in [0, 1]$. The i-th element is given by:

$$a_{i+m} = \sum_{j=0}^{m-1} p_j a_{i+j} \; i = 0, 1, 2, ...2^m - m - 2 \tag{1}$$

The sum elements a_{i+m} can be chosen arbitrary as long as they are either 0 or 1. The sum itself is a summation modulo 2. The sequence length should be even and can then be mapped to a 2d-array by using the product $2^{m/2} + 1 * 2^{m/2} - 1$, which gives for example for $m = 12$ a 63×65 2d-array. The density of the set is also about 0.5 and the autocorrelation-function has a better signal to noise ratio than the one for MURAs. The resulting mask pattern is in general not self supporting, so a fine grid is needed, which is the only disadvantage compared to the MURA-design[Roberto Accorsi, 2001].

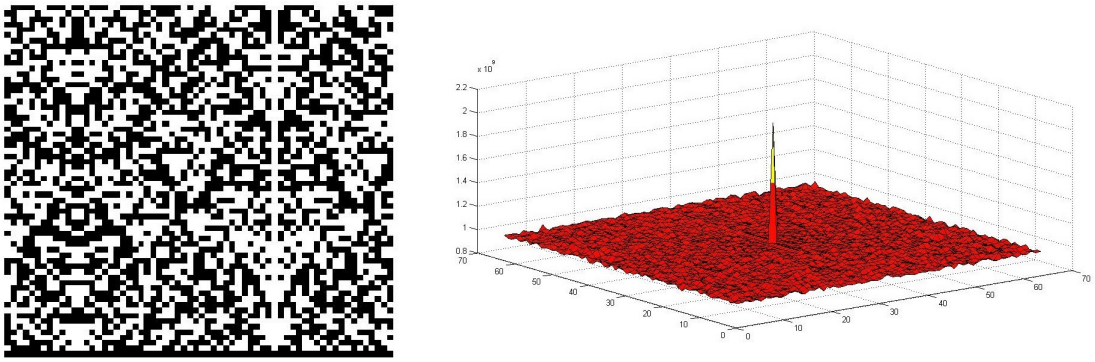

Figure 12: A standard m-sequence-mask with 64 × 64 element size and its typical triangle structure. The mask was cut from an 63 × 65 m-sequence array. The autocorrelation is better than with any other known design.

3.4.3 The Single Pinhole Mask

The Single Pinhole Mask consist of just one hole, most times in the center of the mask. While unsuited for real applications due to the fact, that the Flux hitting the detector is greatly reduced, this mask is excellent for testing the setup and the image reconstruction system.

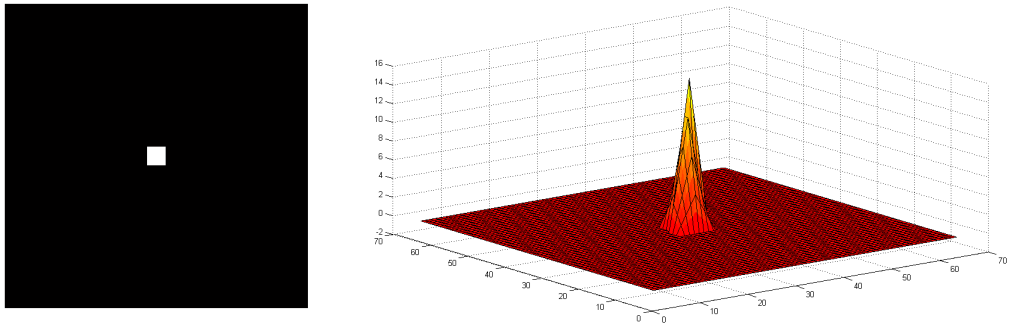

Figure 13: A Single Pinhole Mask. The autocorrelation shows a broader peak.

3.5 Image reconstruction theory

As mentioned before, the real issue with coded mask systems is the computational effort in order to properly decode the sky image onboard a satellite. Several methods have been proposed over the last decades, while the correlation method is the most common by far, due to its excellent results, especially for several sources and its reasonable computation time which only depends on the detector pixel size. The method compares the mask pattern with the detected image to find the best conformity. It makes sense to take a deeper look into the mathematics in the following in order to understand its properties and how this method can be translated into a program reasonably.

3.5.1 Matched cross correlation

The earliest method of decoding is called matched cross correlation where the detected distribution is transformed into a 1d or 2d array F which is correlated with the mask array M while both have the same length, resulting in the sky image S.

$$S(i,j) = F(i,j) \times M(i,j) \tag{2}$$

or expanded:

$$S(j,k) = \sum_l \sum_i F_{li} * M_{j+l,k+i} \tag{3}$$

In the ideal case, F should look exactly like M for a point source while the elements of M are decoded as 1s for transparent pixels and 0s for opaque pixels. The resulting Point spread functions (PSFs) looks like a Pyramid with a peak on top (compare Figure 14). This appearance can be explained by looking at the method itself. The detected vector F is shifted over M while the overlap produces the correlation for every step. When the border of M is reached the overlap goes to 0.

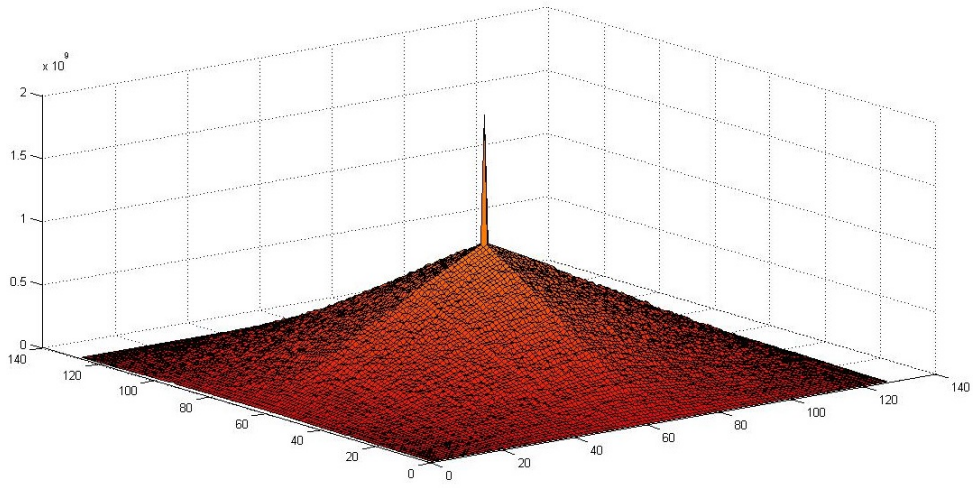

Figure 14: The PSF for a matched 2d autocorrelation with a 65×63 pixel m-sequence pattern. It appears matched correlation should not be used without normalisation in order to cancel out the pyramid.

3.5.2 Mismatched cross correlation

One easy way to circumvent this pyramid shape, is to fill the zeros of the mask-vector with -1 in order to balance the correlation. The average of the sidelobes drops completely to zero and cancels the pyramid, but this method only works for exactly 50% open arrays, because an equal amount of elements with 1 and -1 is needed. In order to overcome this restriction the balanced cross correlation was introduced.

3.5.3 Balanced cross correlation

For values of the open fraction different than 50% simply substituting the opaque mask pixels with -1 is not a solution.Therefore a weighting term w which is derived by the requirement that the sum over all opaque pixels (OP) and transparent pixels (TP) has to be zero, is introduced.

$$\sum_{m_i} = 0 \rightarrow OP + TP * w = 0 \tag{4}$$

We can solve this for w by introducing the total amount of pixels N and the open fraction $OF = \frac{OP}{N}$, which leads us to:

$$w = \frac{-OP}{TP} = \frac{-OP}{N - OP} = \frac{OP}{OP - \frac{OP}{OF}} = \frac{OF}{OF - 1} \tag{5}$$

The balanced mask vector can now be defined as G:

$$G_{jk} = \begin{cases} 1, & \textbf{if } M_{jk} = 1 \\ w, & \textbf{if } M_{jk} = 0 \end{cases} \tag{6}$$

This method ensures that the sidelobes are flattened independent of the pattern used to encode the sky image [Fenimore & Cannon, 1978].
All methods introduced so far have one common disadvantage. Independent of the implementation as a function the calculation speed drops rapidly with higher resolutions as the number of operations n for N Pixels is given by:

$$n = N^2 \tag{7}$$

This means that for example the enhancement from 64×64 Pixels to 128×128 leads to 16 times more calculating steps. As the amount calculating steps is one of the key factors when surveying for GRBs, none of these methods are suitable to achieve fast and precise enough results, as precision directly correlates with detector resolution.

3.5.4 Cross correlation via the Fast Fourier Transform

Another possibility of calculating the cross correlation, is to transform F and M into the Fourier-space and multiply the values of F with the complex conjugate of M and finally inverse transform the resulting array. According to the convolution theorem this operation is equivalent to the cross correlation. The discrete Fourier transform (DFT) G of an array F is defined by:

$$G_k = \sum_{j=0}^{N-1} F_j * e^{-2\pi i \frac{jk}{N}} \tag{8}$$

with N as the length of F and G.
The inverse DFT is defined analogically:

$$F_k = \frac{1}{N} \sum_{j=0}^{N-1} G_j * e^{2\pi i \frac{jk}{N}} \tag{9}$$

The whole process of cross correlation can be described as:

$$Sky\ Image = DFT(DFT(F) * DFT(M)^*)^{-1} \tag{10}$$

This procedure has no direct advantage to the conventional cross correlation calculation, as both require the same amount of operations which is of the order of N^2 and very time consuming.
In 1965 James Cooley and John Tukey published an algorithm that drastically reduces the processing time of the DFT to $(N(log(N)))$[Cooley & Tukey, 1965]. They named it appropriately the Fast Fourier Transform (FFT). The most common form is the Radix-2 algorithm. The first step is to rearrange the DFT into two parts, a sum over the even indices $n = 2m$ and the odd indices $j = 2m + 1$ for every step until $m \leq 2$.

$$G_k = \sum_{j=0}^{N-1} F_j * e^{-2\pi i \frac{jk}{N}} \rightarrow G_k = \sum_{m=0}^{N/(2-1)} F_{2m} * e^{-2\pi i \frac{mk}{2N}} + \sum_{m=0}^{N/(2-1)} F_{2m+1} * e^{-2\pi i \frac{mk}{2N}} \tag{11}$$

By factoring out $e^{-2\pi i \frac{k}{N}}$ the first part can be recognised as the even indexed part of the DFT, which is denoted $E - k$ and the odd indexed part denoted now O_k:

$$G_k = \sum_{m=0}^{N/(2-1)} F_{2m} * e^{-2\pi i \frac{mk}{2N}} + e^{-2\pi i \frac{k}{N}} \sum_{m=0}^{N/(2-1)} F_{2m+1} * e^{-2\pi i \frac{mk}{2N}} = E_k + e^{-2\pi i \frac{k}{N}} \; O_k \tag{12}$$

The periodicity of the DFT gives now: $E_k = E_{k+N/2}$ and $O_k = O_{k+N/2}$.
Therefore, equation 11 can be rewritten as:

$$G_k = \begin{cases} E_k + e^{-2\pi i \frac{k}{N}} \; O_k, & \textbf{for } 0 \leq k \; < N/2 \\ E_{k-N/2} + e^{-2\pi i \frac{k}{N}} \; O_{k-N/2}, & \textbf{for } N/2 \leq k < N \end{cases} \tag{13}$$

The only problem remaining is to calculate the so called twiddle factor $e^{-2\pi i \frac{k}{N}}$.

$$e^{-2\pi i \frac{k+N/2}{N}} = e^{-2\pi i \frac{k}{N} - \pi i} = -e^{-2\pi i \frac{k}{N}} \tag{14}$$

This relation allows us finally to write:

$$G_k = E_k + e^{-2\pi i \frac{k}{N}} \; O_k \tag{15}$$

$$G_{k+N/2} = E_k - e^{-2\pi i \frac{k}{N}} \; O_k$$

This result expresses the DFT of length N recursively in terms of two DFTs with the length $N/2$. The output is a simple combination of E_k and $\pm O_k * e^{-2\pi i \frac{k}{N}}$ which is just a DFT with the length of 2 [Cooley & Tukey, 1965].

Later algorithms as the Radix-4 achieved further speed improvements and are advantageous compared to the the conventional cross correlation calculation. Instruments like the Burst alert Telescope on the Swift-Satellite couldn't have been developed without the usage of the FFT-algorithm as the sky image decoding in time is key to observe GRBs.

4 Hardware development

In the following chapters the software implementation for the cross correlation via FFT will be illustrated. This part represents the main work of the thesis. The complete program was developed with VHDL and uses several Ip-cores of the Xilinx database. The data format is a 1d array with a fixed length of 4096 with 2^{20} Bits single precision points. The decision to use high precision for every point at the cost of FPGA resources was made to ensure that any detector data could be utilized as input without scaling. The array length corresponds to a setup with 64×64 Pixels which is also the resolution of the low energy X-ray detector that has been used for testing purposes. The complete code was duplicated in Matlab for software validation and as a standard reference. Furthermore, five mask-patterns were coded with Matlab in order to produce the test Masks for the X-ray detector. The software was validated on the ISIM[4] testbench and finally tested on a Virtex-4-XS35 FPGA.

4.1 Implementing the cross correlation for an FPGA

4.1.1 Clocking and Reset-management

As the input clocking frequency of the FPGA-Board is 200 Mhz a digital-clock-manager (DCM) is implemented and responsible for creating a stable global clocking signal with a divider of 10 which results in a system-clock of 20 Mhz, which has been chosen in order to fit to the communication interface. As the FPGA starts up the DCM creates the system clock and monitors the length of every cycle. If the clock becomes unstable the DCM sets the locked Signal to 0 and the whole FPGA is reset. Additionally in startup-mode the FFGA holds itself in Reset-state for one second, before releasing to normal operation-mode. This is indicated with all 3 LEDs lighting and then switch off after one second. In Reset Mode a synchronous reset distributed by the TOP-Level stops all operations and the datasets have to be reloaded.

4.1.2 Communication Interface

The communication for incoming mask- and detector data as well as the outgoing processed data is implemented via a small extra communication-board that consists of an standard USB-slave and converts the USB-Signal into the I2C-Bus standard. While the USB-slave is connected to a PC at one side, two wires connect the I2C-Bus to the standard I/Os of the FPGA-board, as one of them functions the Clock-line (SCL) and the other functions as the Data-line (SDA). A wrapper function ensures that every byte transmitted from the PC is acknowledged by the recipient. If the FPGA fails to send an acknowledgement-bit, communication stops immediately. Once a full byte is transmitted, the wrapper sends it up to the FPGA Top-level for further processing. The wrapper function is also responsible to send given bytes bit by bit back to the USB-Board. The whole communication is designed for sending and receiving 4096 packages which represents a 64×64 array mask and detector. A single package is split into 2 bytes before being sent from the PC or back from the FPGA.
The wrapper function and the communication program for the PC used in the setup were written by Henning Wende at the IAAT.

4.1.3 Data preprocessing and RAM Management

Once incoming data have been preprocessed to single bytes by the wrapper function, a package is restored by connecting every two bytes. The acknowledgement if one set of data is either a mask-array or a detector-data-array is implemented with two-byte long headers, 65535 for detector-

[4]The ISIM testbench is a software tool from Xilinx for FPGA-code simulation.

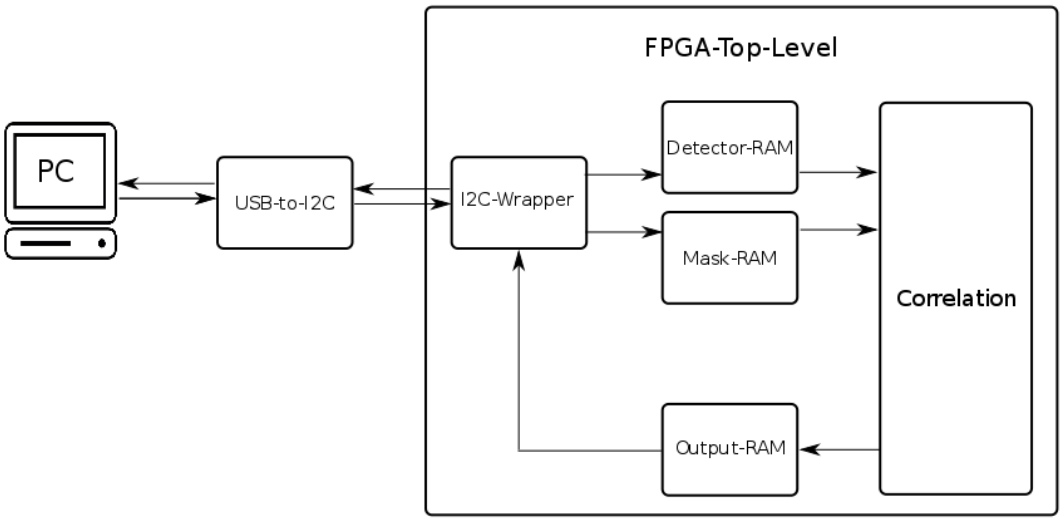

Figure 15: The basic communication architecture of the FPGA implementation. The mask- and detector data is sent from the PC via USB to the communication-board. After the conversion to I2C the wrapper function unpacks the data packages and stores them in the top-level RAMs. After complete transmission of the mask and detector datasets, the correlation process starts and stores the resulting dataset in the Output-RAM. A LED signals that the correlation is finished and the user can now upload the stored result to the PC.

data and 61680 for mask-data. These numbers differ completely from normal data-frames to prevent confusion. The data are then stored into two Input-RAMs, one for detector-data and one for mask-data, while the processed result of the correlation is stored into an Output-RAM. The idea here is that after a mask-dataset has once been sent, detector-datasets and result-datasets can be sent continuously without any reloading of the mask-dataset necessary.

4.1.4 The FFT cross correlation

Once the Detector-RAM and the Mask-RAM are completely loaded, which is signalled by LED1 for the Detector-RAM and LED2 for the Mask-RAM, the correlation process starts. The Detector- and Mask-Data is first loaded into two sub-routine-RAMs, subsequently fourier-transformed by a FFT-IP-core and then complex multiplied. The result is inverse fourier-transformed and finally the absolute value for every frame is calculated. The correlation-process has its own sub-routine-RAMs in order to store in between results locally. Once the correlation is finished and completely written in the Output-RAM the LED3 is switched on. Now the transmission of the result-Dataset can be started from the PC. If the validation package, that follows the last data-package is sent successfully all LEDs are switched off. The main sequence of the correlation is shown in Figure 17.

The three basic operations, namely the fourier-transformation, the complex multiplication and the calculation of the absolute value are coded as subroutines.

1. The fourier-transformation is done by a LogiCORE IP Fast Fourier Transform 7.1. The IP-core uses the Cooley-Tukey algorithm as described in Chapter 3.5.4. It can compute frame lengths of $N = 2^m$ with $m = 3 - 16$ and perform direct and inverse FFTs. From the several possible architectures options the Radix-4 has been chosen, as it features the best combination of processing speed and space requirements. The testbench results show a 50 % calculation step reduction for Radix-4 algorithm compared to the Radix-2 algorithm. The IP-core offers two different scaling options: either a fixed scaling schedule after every step, or scaling automatically by using the block floating point format. The second option offers the advantage that scaling is only performed if necessary and all bits of one data-package are used instead of a fixed cut-off after a certain bit-length. The precision of the result is strongly dependent on the amount of phase factor bits used in the implementation as shown in Figure 16.

2. The complex multiplication uses several IP-cores for basic math functions, as an adder-subtractor and a multiplicator.

3. The absolute value calculation works similarly as the complex multiplication subroutine, but it uses a Cordic-Core additionally for square-root calculations.

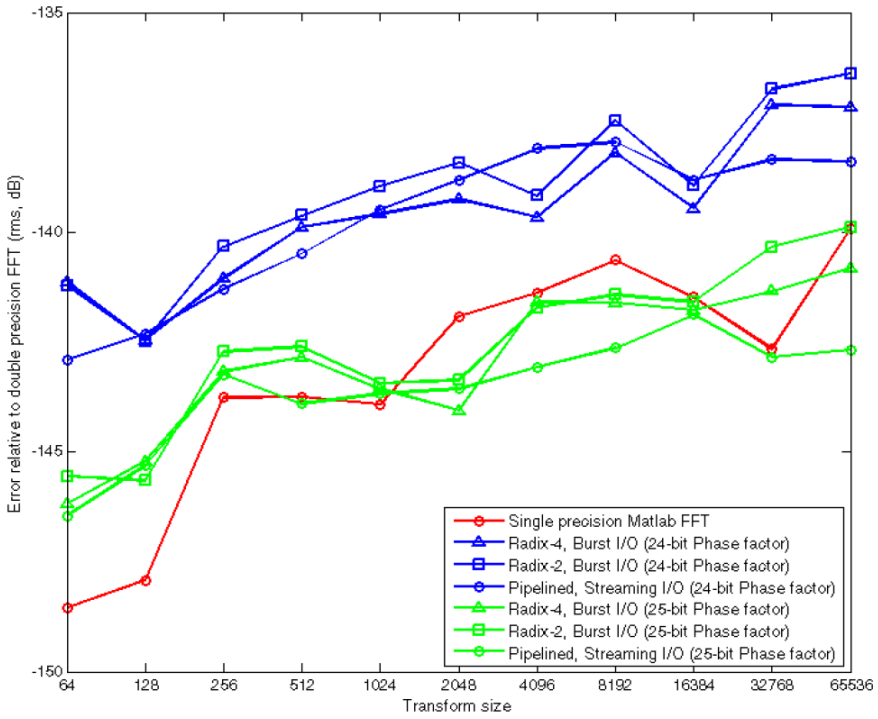

Figure 16: The diagram compares the precision of the FFT-calculation of different IP-core architectures with a Matlab FFT function. For the transform size of 4096 packages the diagram shows an even higher precision for the Radix-4 architecture with a phase factor of 25 bits, than for the Matlab FFT function. With a 24 bit phase factor the Matlab FFT function already produces results with a significant higher precision than the FFT-IP-core. In this work the maximum phase factor can only be 20 bits, which explains the poor results for low signal to noise ratio correlations. *image and source: Xilinx LogiCORE Database*

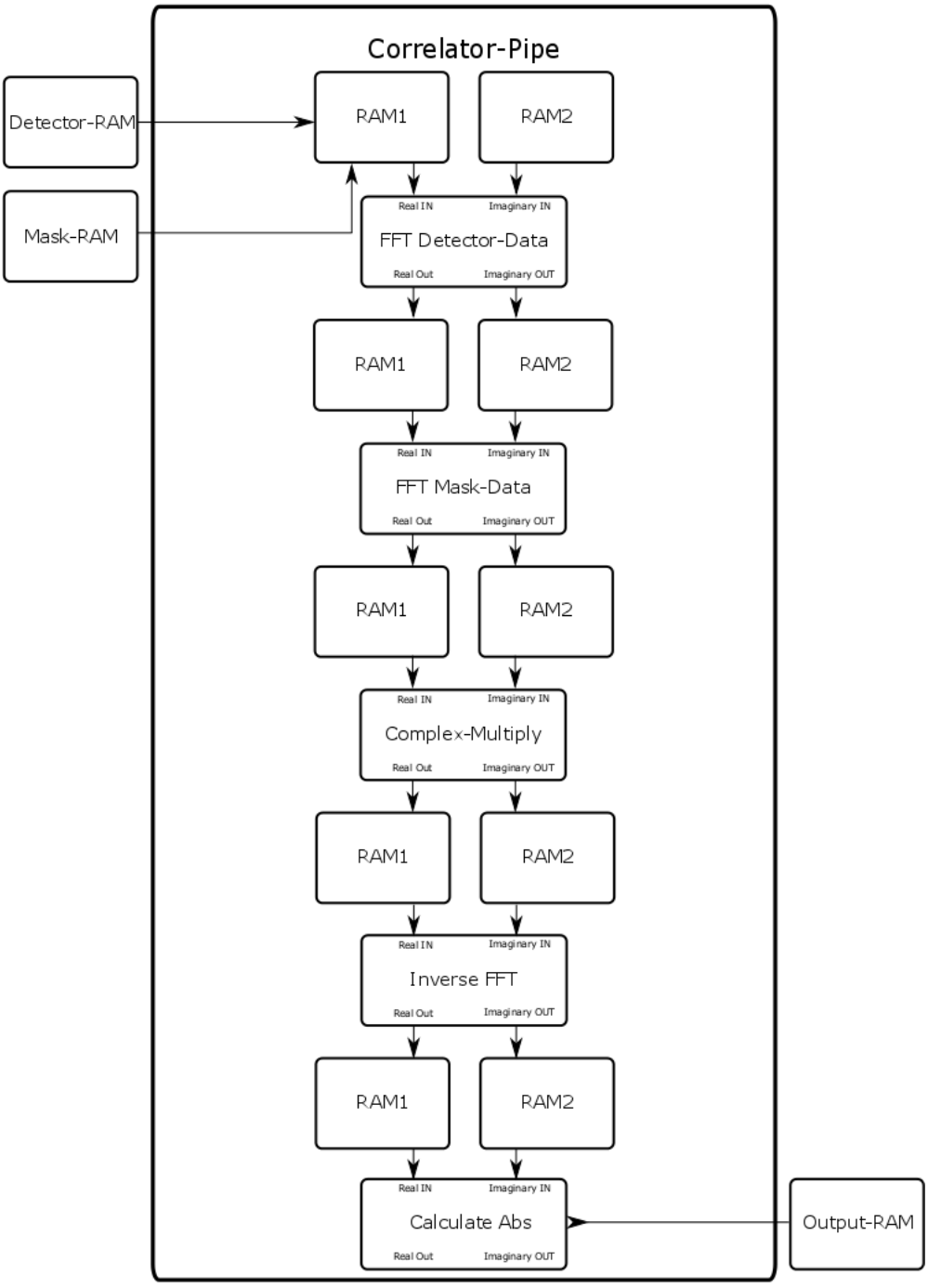

Figure 17: The complete calculation process of the cross-correlation. The FFT computation and the multiplications are done with own subroutines.

4.2 Matlab implementation for reference results

The whole autocorrelation function via FFT has also been implemented with Matlab. The Data runs through the same steps as in the FPGA implementation. The only difference is the format of single data-frames. While one frame must not be bigger than 20 Bits for the FPGA implementation and the format is fixed point numbers, which means that the number of digits behind the radix point cannot be changed, none of these constraints apply to Matlab. This means in practice that Matlab should deliver results with higher precision than the FPGA-implementation as long as less than 25 Bits for the phase factor are used as shown in Figure 16.

4.2.1 Mask Designs for the test setup

The mask-patterns for the different test-masks are also generated with Matlab. The code for the mask-patterns is shown in the appendix. The layouts then were used as models to produce aluminium masks for a test-setup with a low energy X-ray detector. The following patterns were produced and tested:

1. An m-sequence mask
2. A MURA mask by concatenating four 32 x 32 pixel MURA-patterns
3. A pinhole Mask with a 4 x 4 pixel pinhole

All three masks apply to following parameters:

1. The resolution is 64 x 64 pixels
2. The dimension is 4 cm width and 4 cm height for the pattern itself
3. The thickness is 150 μm for the MURA mask and the pinhole mask and 250 μm for the m-sequence Mask
4. The height and width for one Pixel is $\frac{40\,\mathrm{mm}}{64} = 0,625\,\mathrm{mm}$
5. A grid had to be implemented for the MURA mask and the m-sequence mask, which shrinks the size of transparent pixels to $0,5\,\mathrm{mm}$

Additionally a mask with a random pattern has been designed in order to compare the quality of the autocorrelation functions.

5 Validation and Testing

During the development process the whole implementation had to pass several validation stages and was finally tested with real detector data. The first step of validation is a logical test of the subroutines performed with the Isim-testbench[1] , which is a comfortable build in testing tool for VHDL-designs. It simulates the synthesized design while every parameter and signal can be monitored.
If every subroutine works correctly the process can be repeated for the whole design in order to proof that the single subroutines work together correctly.
For the final stage of validation the FPGA is configured with the synthesized design and the same set of data is sent as detector-data and as mask-data as well, in order to test the design with an autocorrelation. This part of validating brings the difficulty that signals cannot be observed as easily inside the FPGA as with a testbench environment. To circumvent this problem, Chipscope, a virtual multichannel-analyser has been implemented and used to find and solve communication problems.
In the following, the test results of the autocorrelation functions as well as for the measured detector-data will be presented. The The Signal to Noise Ratio (SNR), which is defined here as $SNR = \frac{P_{signal}}{P_{noise}}$ with P_{signal} for the correlation peak and P_{moise} for the highest sidelobe, will be also shown and compared for both implementations.

5.1 Autocorrelation functions of different Masks

Testing the autocorrelation function fulfils two main purposes. It verifies the quality of the mask used and is additionally useful for comparing the FPGA-implementation with the Matlab reference. Therefore for all masks both results will be shown and discussed.

5.1.1 The m-sequence Mask

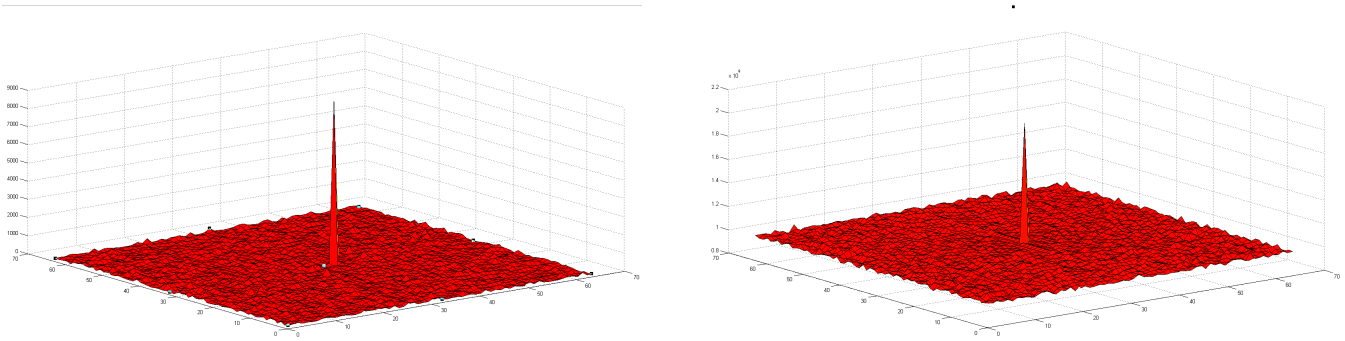

Figure 18: The autocorrelated function of the m-sequence mask. The FPGA results on the left, the Matlab results on the right.

The results for the m-sequence mask show a very sharp delta function for both programs in Figure 18. There are no big differences between the results, the SNR is even better for the FPGA implementation with a SNR of 32,4 compared to a SNR of 24,6 for the Matlab implementation. Besides no visible sidelobes are appearing, which approves that this mask type has no self repeating patterns.

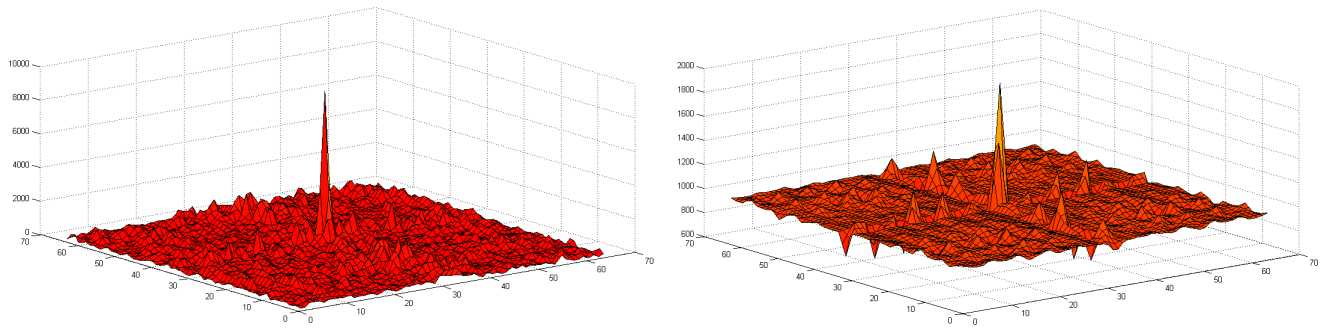

Figure 19: The autocorrelated function of the MURA mask. The FPGA results on the left, the Matlab results on the right.

5.1.2 The MURA Mask

For the MURA mask the result is a delta function with a SNR of 7,9 for the FPGA program and SNR of 4,4 for the Matlab program. Both implementations produce sidelobes to some extend as the distributivity of them is the main difference between the two plots (compare Figure 19). For the Matlab result the sidelobes only emerge around the X-axis and Y-axis along the correlation peak, which displays that this mask was built by concatenating 32 x 32 MURA Masks four times. The FPGA result instead shows a more random distribution of the sidelobes which are in average smaller than the Matlab version. This can be attributed to the rounding and truncation constraints of the FPGA design.

5.1.3 The single pinhole Mask

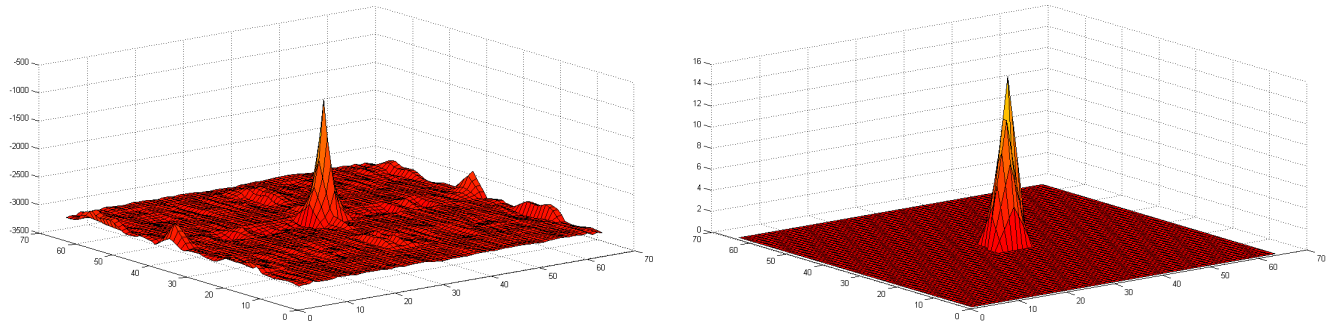

Figure 20: The autocorrelated function of the single pinhole Mask. The FPGA results on the left, the Matlab results on the right.

For the single 4 x 4 pixel pinhole both results show a clear peak in the center (compare Figure 20). The Matlab plot shows absolutely no sidelobes so no SNR could be calculated, while the FPGA plot has sidelobes to some extend around the X-axis and Y-axis along the correlation peak and has a SNR of 6,3. Again the necessity of rounding due to limited workspace in the FPGA design is responsible for this behaviour.

[1] [Xilinx, 2011]

5.2 Correlation Results for different masks

After the production of the aluminium masks, all three of them were placed one after another in front of the low energy X-ray Detector as shown in Figure 22 and exposed to X-ray emission. Two different isotopes were used as sources. The hitmap of the detector shows the best results with the Fe-55 source and this data have been used for the correlation tests.

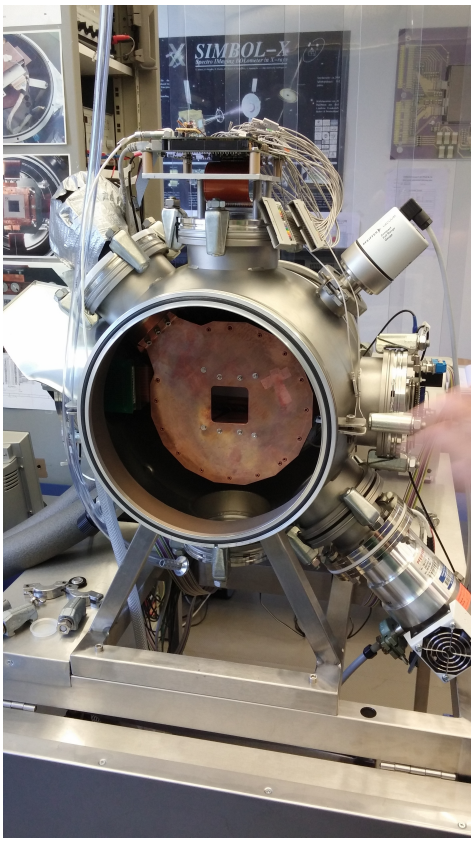

Figure 21: The CANDELA setup with the low energy X-ray detector (LED) in the center behind a copper cooling device.

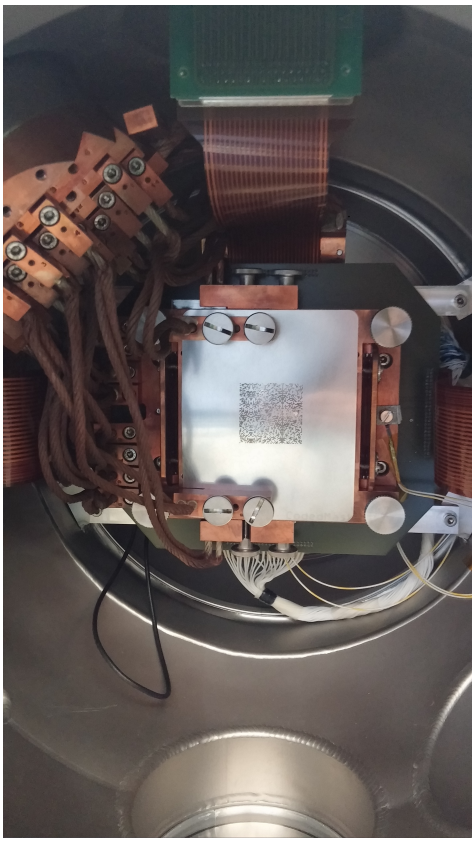

Figure 22: The LED with an m-sequence mask placed directly in front of the detector.

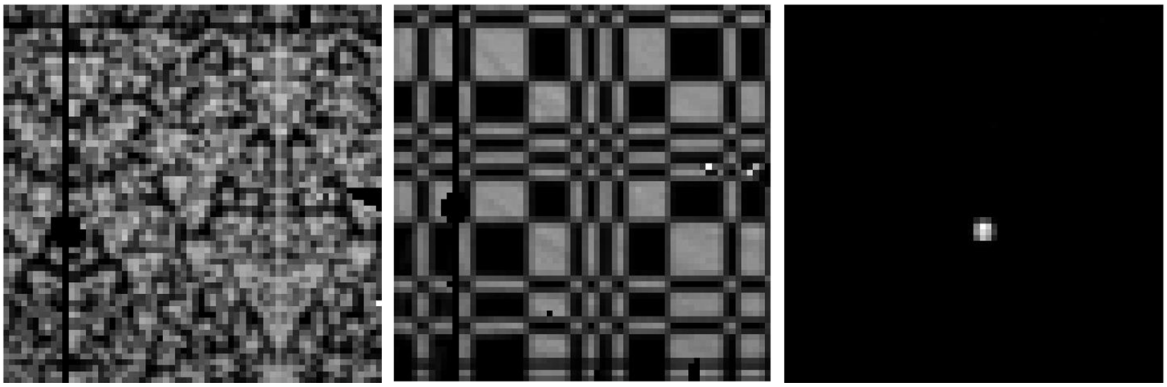

Figure 23: The diagram shows the hitmaps for the three different masks. On the left the hitmap for the m-sequence mask. In the middle the hitmap for the MURA mask. On the right the hitmap for the single pinhole mask. While the pattern of the m-sequence mask can be recognised, the hitmap of the MURA mask shows a zoomed image of the pattern, which can be referred to the usage of too large dimensions for the mask.

5.2.1 The m-sequence Mask

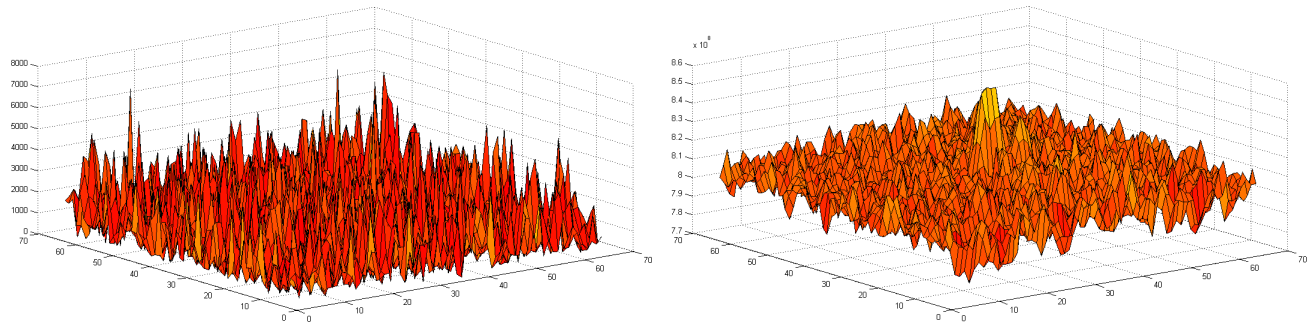

Figure 24: The cross correlation of the m-sequence mask. The FPGA results on the left, the Matlab results on the right.

The plots show that the FPGA Data seems to be random and has no clear correlation peak, but the Matlab data shows a clear correlation peak (compare Figure 24). As already described in Chapter 4.1.4 the necessary scaling in the FPGA design is responsible for this bad result. Also in the Matlab plot has a very weak correlation peak with a SNR of 1,38. This can be explained by the non optimal setup of the optical design as the mask pattern is not perfectly aligned with the Detector. Additionally the Detector has more than 5 % defect pixels that do not respond to any input signal, which is not taken into account in the analysis [Maier, 2015].

5.2.2 The MURA Mask

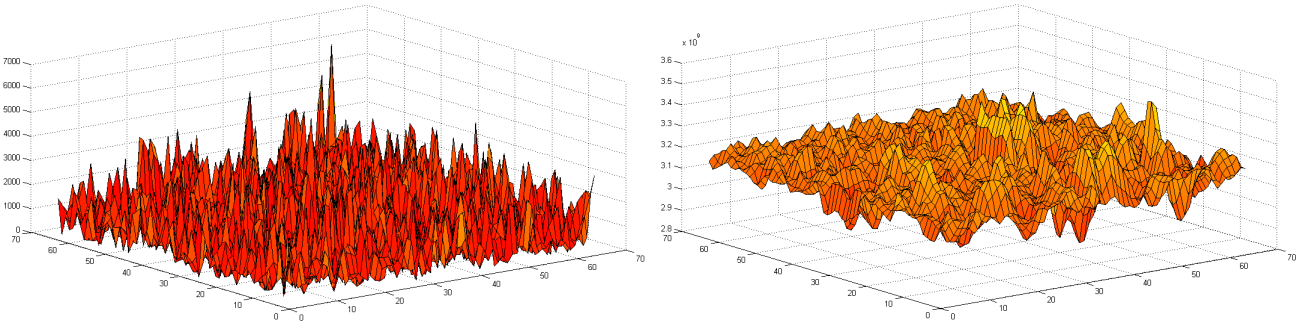

Figure 25: The cross correlation of the MURA mask. The FPGA results on the left, the Matlab results on the right.

Similar to the results with the m-sequence mask the FPGA data shows no clear correlation in Figure 25. The Matlab Data has a broadened correlation peak in the center with a SNR of 1,13. The main reason for this even worse result compared to the m-sequence mask is a production mistake of the mask itself. Instead of having the same size like the detector it was produced 50 % larger which explains the zoom effect on the hitmap in Figure 23.

5.2.3 The Pinhole Mask

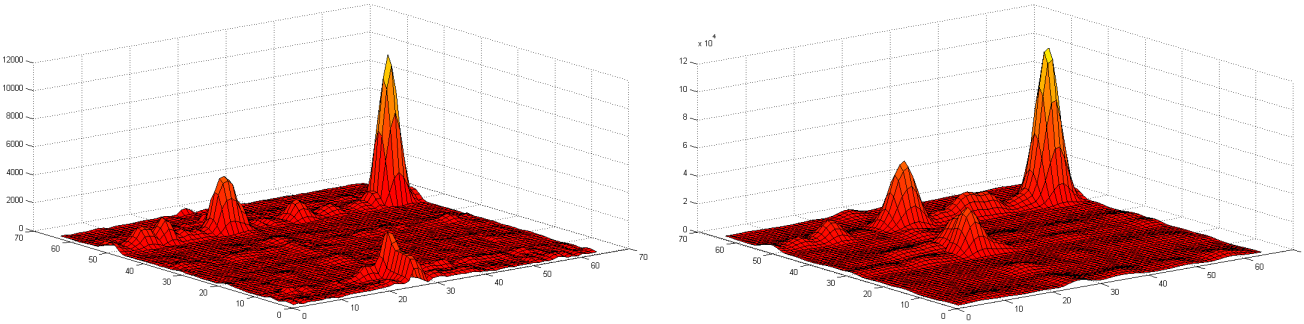

Figure 26: The cross correlation of the Pinhole Mask. The FPGA results on the left, the Matlab results on the right.

The results for the Pinhole Mask show good correlation peaks for both Data sets (compare Figure 26). Interestingly the sidelobes are higher for the Matlab data with a SNR of 2,44 compared with a SNR of 2,63 for the detector data. Both plots show that the Fe-55 source is not aligned exactly in front of the the Mask-Detector-setup as the peak is shifted from the center.

5.3 Test Results for processing speed

As mentioned before, one of the critical parameters is processing speed. The aim for this thesis was to at least match the processing speed of the BAT on the Swift-mission which is 17 s from detecting a GRB to the final trigger decision for a 128×256 pixel size detector, while it takes 12 s for the digital signal processor to generate the sky image alone [Barthelmy *et al.*, 2005]. The current time of the correlation-process of this work is shorter than 15 ms while the current clock-speed is only at 20 Mhz. The maximum clock-speed is theoretically 220 Mhz while the current design has also been tested with 100 Mhz, which equals 3 ms processing time.
Additionally, the forward FFTs could be pipelined and more importantly one could delete the square-root function for the absolute value of the result as this function alone needs over 50% of the processing time. Also bigger pixel sizes only lead to a proportionally longer processing time as basic math functions behave linearly and the speed of the FFT refers to $(N(log(N)))$ as shown in Chapter 3.5.4.

6 Outlook

The current state of implementation could be a good starting point to design a complete image reconstruction device for the WFM of the LOFT mission. As this thesis has shown, sufficient calculation speed can be achieved even without any speed optimisation.
The project can be used for detector-data with different pixel sizes without major difficulties. But there is an upper limit as the standard FFT-IP-cores do not accept pixel sizes exceeding 256 x 256, which is more than enough for a single camera of the WFM with its 1040×16 element size. Another difficulty occurs when the Mask pixel size differs from the Detector pixel size, which is also a general problem with cross correlation, but it can be prevented by proper padding of the input data to an equal length.
The biggest weak-point of the current implementation is the low precision with weak correlations which can be matched by using more bits per frame to achieve less rounding and truncation errors. It would be interesting to analyse results from real detector-data including an observed GRB in order to find out how much rounding is acceptable as RAM-Space is limited for FPGAs.

References

[Amati, L, 2003] Amati, L. 2003. The Bepposax Revolution in Gamma-Ray Burst Science.

[Barstow M. et al, 1990] Barstow M. et al. 1990. XUV wide field camera for ROSAT.

[Barthelmy *et al.*, 2005] Barthelmy, Scott D., Barbier, Louis M., Cummings, Jay R., Fenimore, Ed E., Gehrels, Neil, Hullinger, Derek, Krimm, Hans A., Markwardt, Craig B., Palmer, David M., Parsons, Ann, Sato, Goro, Suzuki, Masaya, Takahashi, Tadayuki, Tashiro, Makota, & Tueller, Jack. 2005. The Burst Alert Telescope (BAT) on the SWIFT Midex Mission. *Space Science Reviews*, **120**(3-4), 143–164.

[Brandt S. et al, 2013] Brandt S. et al. 2013. Observing GRBs with the Wide Field Monitor.

[Brandt S. et al, 2014] Brandt S. et al. 2014. The design of the wide field monitor for LOFT.

[Cooley & Tukey, 1965] Cooley & Tukey. 1965. An Algorithm for the Machine Calculation of Complex Fourier Series. *Mathematics of Computation, Volume 19, Issue 90(Apr.,1965),297-301.*

[Dean, 1983] Dean, A. J. 1983. Imaging systems using modulation and coded aperture masks. *Advances in Space Research*, **3**(4), 73–82.

[Fenimore & Cannon, 1978] Fenimore, E. E., & Cannon, T. M. 1978. Coded aperture imaging with uniformly redundant arrays. *Applied Optics*, **17**(3), 337.

[Friedman, 1951] Friedman, H.; Lichtman, S. W.; Byram E. T. 1951. Photon Counter Measurements of Solar X-Rays and Extreme Ultraviolet Light.

[Jagoda, 1972] Jagoda, N.; Austin, G.; Mickiewicz S.; Goddard R. 1972. The UHURU X-Ray Instrument.

[Kimberly Kowal Arcand, 2012] Kimberly Kowal Arcand. 2012. *Chandra Telescope System.*

[Maier, 2015] Maier, Daniel. 2015. Development of a stacked detector system and its application as an X-ray polarimeter.

[Peterson, 1975] Peterson, L. 1975. Instrumental technique in X-ray astronomy.

[R. J. Procter, G. K. Skinner, A. P. Willmore, 1978] R. J. Procter, G. K. Skinner, A. P. Willmore. 1978. The design of optimum coded mask X-ray telescopes.

[Roberto Accorsi, 2001] Roberto Accorsi. 2001. Design of near-field Coded Aperture Cameras for High-Resolution Medical and Industrial Gamma-Ray-Imaging.

[Schanne Stephane. et al, 2014] Schanne Stephane. et al. 2014. The LOFT Burst Alert System and its Burst On-board Trigger.

[Seward F.D. Charles P.A. , 2010] Seward F.D. Charles P.A. . 2010. Exploring the X-ray Universe.

[Tauris & van den Heuvel, 2006] Tauris, T.M., & van den Heuvel, E.P.J. 2006. Formation and Evolution of compact stellar X-ray sources.

[Ubertini *et al.*, 2003] Ubertini, P., Lebrun, F., Di Cocco, G., Bazzano, A., Bird, A. J., Broenstad, K., Goldwurm, A., La Rosa, G., Labanti, C., Laurent, P., Mirabel, I. F., Quadrini, E. M., Ramsey, B., Reglero, V., Sabau, L., Sacco, B., Staubert, R., Vigroux, L., Weisskopf, M. C., & Zdziarski, A. A. 2003. IBIS: The Imager on-board INTEGRAL. *Astronomy and Astrophysics*, **411**(1), L131–L139.

[Wolter Hans, 1952] Wolter Hans. 1952. Spiegelsysteme streifenden Einfalls als abbildende Optik für Röntgenstrahlen.

[Xilinx, 2011] Xilinx. 2011. ISE Simulator (ISIM) In-Depth Tutorial.

[Zand, Johannes Joseph Marie in 't, 1992] Zand, Johannes Joseph Marie in 't. 1992. *A Coded-mask imager as monitor of galactic x-ray sources.*

[Zane S., 2014] Zane S. 2014. LOFT — Large Observatory for X-ray Timing.

[Zane S. et al, 2014] Zane S. et al. 2014. The large area detector of LOFT: the Large Observatory for X-ray Timing.

Appendix

1. Code for the MURA mask

```
function [Mask] = murra(in)

for j = 1:1:in-1
    for b = 1:1:in-1
        if j == 0;
            out = 0;
        else
          cp = cpfunc(in, j)*cpfunc(in, b);

          if ((b == 0 & j == not(0)) | (cp == 1))
              out = 1;
          else
              out = 0;
          end
          Mask(j, b) = out;

        end
    end
end
Mask(j, b) = out;
I = mat2gray(Mask);
imshow(I);
```

2. Code for the m-sequence mask

```
function [M2] = lfsr2

shiftRegLength = 12;

shiftReg = [0,0,0,0,0,0,0,0,0,0,1,0];

for i = 1:1:4096


bit = (xor(xor(xor(shiftReg(12),shiftReg(11)),shiftReg(10)),shiftReg(4)) & 1);
x = mod((i -1),65);
y = mod((i-1),63);
out3(i) = mod(bi2de(shiftReg),2) ;
s = circshift(shiftReg,[0,1]);
%Insert that value in the beginning and shift the rest to the right
shiftReg = [bit s(2:12)];
if out3(i) == 0
    Mask(x +1 ,y +1 ) = 1000;
else
    Mask(x +1,y +1) = 0;
end

end
lfsrmask = reshape(out3,[sqrt(length(out3)),sqrt(length(out3))]);
I = mat2gray(lfsrmask);
M1 = circshift(rot90(Mask,1),[17,1]);
for x= 1:1:64
    for y= 1:1:64

        if x == 64;
            M2(x,y) = 0;
        else
        M2(x,y) = M1(x,y);
        end;
    end;
end;
I = mat2gray(M2);
imshow(I)
```

3. Code for the single pinhole mask

```
function [PMask] = pointmask
in = 64

for j=1:1:in
    for b=1:1:in
        if (j == 31 | j == 32 | j == 33 | j == 34) & (b == 31 | b == 32 | b == 33 | b
            PMask(j,b) = 1;
        else
            PMask(j,b) = 0;
        end;
    end;
end;

I = mat2gray(PMask);
imshow(I);
```

Declaration

I declare that I have developed and written the enclosed bachelor thesis completely by myself, and have not used sources or means without declaration in the text. Any thoughts from others or literal quotations are clearly marked. The bachelor thesis is not used in the same or in a similar version to achieve an academic grading or is being published elsewhere.

Location, Date

Signature

Acknowledgements

I wish to express my sincere thanks to Prof. Santangelo, the head of the high energy astrophysics working group, for providing me with the necessary technical equipment and making my bachelor thesis possible.
I also like to thank Michael Gschwender for laying my foundations in hardware programming in the first weeks. I would also like to show my gratitude to Dr. Daniel Maier, who made the practical tests with the LED-detector possible and spent several days measuring.
I am also grateful for the help and support of Henning Wende, who implemented the communication protocol for the FPGA and also helped me several times to solve conceptual problems in my implementation. He invested an extensive amount of time explaining me deeper concepts of VHDL-coding and ensuring I understand why these concepts are important.
Finally I want to thank Dr. Chris Tenzer for his excellent supervision and support. Not only he corrected my thesis several times, he even helped me with the test result analysis during his free time on a bright Sunday afternoon. Additionally he put in a lot of effort to teach me the basics of VHDL-programming.